Article

Disturbance Interval Observer-Based Robust Constrained Control for Unmanned Aerial Vehicle Path Following

Yaping Song, Kenan Yong * and Xiaolong Wang

College of Automation Engineering, Nanjing University of Aeronautics and Astronautics, Nanjing 211106, China
* Correspondence: yongkenan@nuaa.edu.cn

Abstract: This work presents a robust constrained path-following control scheme for the unmanned aerial vehicle (UAV) under wind disturbances. Through appointing the projection from the UAV to the path, the Serret–Frenet frame is introduced to reduce the complexity of the path-following problem. Specifically, the disturbance interval observer is employed to generate the interval of the wind disturbances. Then, the path-following control design is presented based on the dynamic surface control technique, and the auxiliary system is adopted to deal with the command limitation during the design process. Accordingly, the stability of the closed-loop system is analyzed. The effectiveness of the developed control scheme is demonstrated using numerical simulations.

1. Introduction

Unmanned aerial vehicles (UAVs) have been important research objects of autonomous systems. They have been widely used in autonomous environmental monitoring, target searching, surveillance, and reconnaissance. These tasks generally require UAVs to cruise along a prescribed path [1], which also lays a technical foundation for more complex tasks such as ground-moving vehicle tracking. Compared with multi-rotor UAVs, the advantages of fixed-wing UAVs, including larger payloads, faster speed, and more durable endurance, make them more suitable for long-distance missions. However, due to the aerodynamic properties of the fixed-wing aircraft, the mission performance of UAVs is highly dependent on the atmospheric environment [2]. Particularly, wind disturbance is an essential condition affecting that performance. Thus, the position tracking of UAVs under wind disturbances, which is also the topic of this work, is a crucial issue to investigate.

There are two classical methods for fixed-wing UAVs to cruise and fly along a fixed path, i.e., trajectory tracking control [3,4] and path-following control [5,6]. The differences between them have been discussed in [7,8]. Specifically, trajectory tracking requires the UAV to arrive at a specific location at the predetermined time, while path following only requires the UAV's position to converge to a prescribed path. In other words, for the path-following control, the air speed of the UAV is controlled independently, which reduces the complexity of the flight control system. It can prevent the UAV from stalling when flying downwind and keep the dynamics of the UAV in the linear region of trim points [6].

Most autonomous systems have the requirement of path following, and there are two design methodologies, geometric and control, to solve the path-following problem. For example, the virtual target point (VTP) is a classical geometric method [9,10]. The vector field (VF) technique is one of the popular geometric methods [11], which aims to calculate the desired heading of the UAV according to the relative distance from the straight line or circular reference path. The VF-based method is widely used in many scenarios [12], including complex stellar curves [13]. Meanwhile, there are many path-following methods based on the control methodology. The Serret–Frenet frame transformation is used to define the error dynamics between the UAV and the reference path so as to apply different control technologies to stabilize

the error dynamics [14,15]. A linear model predictive control method for guidance law design was presented, where the UAV dynamics were linearized at a specific working point [16]. An improved adaptive integrated line-of-sight (LOS) guidance method was proposed for unmanned surface vehicles (USVs) to eliminate the adverse effects of side-slip angle [17]. Similarly, by using the LOS guidance method, an internal model control was proposed to estimate the side-slip angle [18]. An integrated model was constructed based on the dynamics of both the LOS variables and the acceleration components, and a target-tracking control method was proposed [19]. Based on the LOS method and the Kalman filter method, a passive anti-disturbance guidance law similar to the robust control technology of the H_∞ method was proposed for missiles [20]. A USV guidance and control integration technology was realized based on the Serret–Frenet coordinate system, and a heading control strategy and reference point speed control method were proposed based on the non-linear backstepping method [21]. However, for the studied UAVs, the path-following problem becomes more complex, and the above-mentioned method may be not completely applicable to UAVs. In the process of designing the path-following controller of the UAV, issues such as command limitation and input saturation should be addressed [13]. The nested saturation theory was used to solve the input saturation problem, and a strict convergence proof was given by using the LaSalle theory [22]. The constraints on rolling and flight path angles were explicitly considered in [6], and the path-following guidance law was proposed for the UAVs using the nested saturation theory.

Meanwhile, the path-following problem of the UAVs always assumes that the heading angle is equal to the flight path angle of the fixed-wing aircraft [11,23], while this assumption is only applicable to the scene without wind disturbance. For small UAVs, ambient winds may cause significant differences in reference paths between the wind coordinate frame and the inertial coordinate frame. To eliminate this restriction, many improved methods have been developed [6,24,25], in which the wind information had to be available. One way to eliminate the effects of wind disturbance is to use course angle and ground speed for the path-following control design [26]. In [11,27], the ground speed and the course angle were employed to design a path-following controller instead of the airspeed and the heading angle. However, in practice, the UAV's course angle and ground speed from low-cost GPS modules may be degraded. Therefore, the UAV's heading angle and airspeed for path-following control can be better applied to low-cost small fixed-wing UAVs.

Another feasible solution is to use the adaptive approximation and/or disturbance observer to obtain wind disturbance online and introduce compensation in controller design for the wind disturbance. A sliding-mode active disturbance rejection control scheme was proposed for the trajectory tracking control of four-rotor UAVs [28]. To address the path-following problem of a four-rotor UAV with constant disturbance, a nonlinear adaptive state feedback controller was proposed [29]. A path-following control scheme for the adaptive estimation of wind disturbance was proposed based on adaptive backstepping [30]. Notably, many scholars use disturbance observers (DOBs) to solve the anti-disturbance control problem, including the path-following one. A sliding-mode control scheme was proposed for a class of nonlinear systems based on a disturbance observer [31]. An adaptive dynamic surface control strategy based on a disturbance observer was proposed for the near-space vehicle with multi-input and multi-output attitude motion in the presence of external disturbances [32]. Recently, some novel algorithms have been applied to some practical problems. A neuro-adaptive learning method was introduced for the problem of constrained nonlinear systems with disturbance rejection [33]. Through using the Serret–Frenet frame and the VTP, a nonlinear disturbance observer was designed to estimate and compensate for the wind disturbance [34]. A robust discrete-time fractional-order tracking control scheme based on a discrete-time disturbance observer was proposed for UAV systems with unknown bounded variation disturbances [35]. In [36], two novel continuous integral robust control algorithms with asymptotic tracking performance were constructed for a class of high-order uncertain nonlinear systems with matched and unmatched composite

disturbance. Although the stability of these estimators can be guaranteed, the performance of disturbance estimation may not be satisfactory enough, especially before the estimation error exists or the estimation error completely converges. This characteristic may cause people to doubt whether the disturbance can be fully compensated. More recently, the disturbance interval observer (DIOB), which was proposed in [37,38], has gradually become one of the important methods to solve the anti-disturbance control problem. However, as a new technology, the DIOB is still rarely used in UAV flight control design, and more efforts are needed for the practical application.

With the above motivation, a DIOB-based robust constrained control scheme is developed for the path-following UAV under wind disturbances and command limitation. The main contributions of this work are summarized as follows:

- A specific DIOB is developed for the position kinematics of the UAV. Through the appropriate use of the information in the inertial framework, it is capable of providing interval estimation of the wind disturbances and providing more robustness for the feedforward compensation;
- The Serret–Frenet frame is introduced to transform the path-following problem of the UAV into a general stabilizing control one. By improving the dynamic surface control technique, the resulting flight control design can address the non-affine nonlinearity of the UAV kinematics;
- An auxiliary system is employed to address the command limitation on the heading angle of the UAV. Specifically, the stiff saturation nonlinearity is replaced with a saturation-like smooth nonlinear, which guarantees the differentiability of the virtual control law.

The structure of this paper is as follows: The second section describes the path-following problem of the UAV. The third section presents the design of the DIOB and the path-following control and then proves the stability of the closed-loop system. The fourth section verifies the effectiveness of this path-following method based on numerical simulations.

Symbol Description [2]:

- $\mathbb{R}$ denotes the real number set, $\mathbb{R}^n$ is an n-dimensional Euclidean space; meanwhile, $\mathbb{R}_{\geqslant 0} = \{a_n \in \mathbb{R} | a_n \geqslant 0\}$ and $\mathbb{R}_{>0} = \{a_n \in \mathbb{R} | a_n > 0\}$;
- For the given matrix or vector $A_n = [A_n^{i,j}]$, define $|A_n|^* = [|A_n^{i,j}|]$, $A_n^+ = 0.5(A_n + |A_n|^*)$ and $A_n^- = A_n^+ - A_n$;
- For given matrices or vectors $A_n = [A_n^{i,j}]$ and $B_n = [B_n^{i,j}]$, $A_n \geqslant B_n$ denotes that for any i,j have $A_n^{i,j} \geqslant B_n^{i,j}$;
- For the given real symmetric matrix A_n, $A_n \succ 0$ and $A_n \prec 0$ represent that the matrix A_n is positive or negative definite, respectively;
- For the given real symmetric matrix A_n, $\lambda_{\max}(A_n)$ represents the maximum characteristic root of matrix A_n;
- For the given matrix or vector A_n, A_n^{T} denotes the transpose matrix of A_n;
- For the given vector A_n, $||A_n||$ denotes the Euclidean norm of A_n.

2. Problem Formulation and Preliminaries

2.1. UAV Kinematics in Inertial Frame

This paper aims to solve the path-following problem of fixed-wing UAVs under wind disturbance. For convenience, only the kinematic model of the fixed-wing UAV is considered. At the same time, it is assumed that the UAV maintains a constant altitude and

airspeed. Then, we obtain a suitable fixed-wing UAV kinematic model that is modeled in the inertial and body frames, i.e., $\mathcal{I}$ and $\mathcal{B}$, as previously described [1,25].

$$
\begin{cases}
\dot{p}_x = V_a \sin \psi + w_x \\
\dot{p}_y = V_a \cos \psi + w_y \\
\dot{\psi} = \frac{g}{V_a} \tan \phi \\
\dot{\phi} = b_\phi (u - \phi)
\end{cases}
\tag{1}
$$

where $p_x, p_y \in \mathbb{R}$ are the positions of the UAV in the inertial frame; V_a is the airspeed; $\psi \in \mathbb{R}$ and $\phi \in \mathbb{R}$ are the UAV's heading and rolling angles, respectively; $u \in \mathbb{R}$ is the control input; $w_x \in \mathbb{R}$ and $w_y \in \mathbb{R}$ are the velocities of the wind disturbance in the inertial frame; $b_\phi > 0$ is a constant depending on the properties of the attitude controller; and g is the acceleration of gravity.

The variables involved in the kinematics (1) are shown in Figure 1, where $x_\mathcal{B}$, $y_\mathcal{B}$, and $z_\mathcal{B}$ are the axes of the UAV body frame, $O_\mathcal{B}$ is the coordinate origin of the body frame, and $x_\mathcal{I}$ and $y_\mathcal{I}$ are the axes of the inertial frame with $P = [p_x, p_y]^\mathrm{T}$.
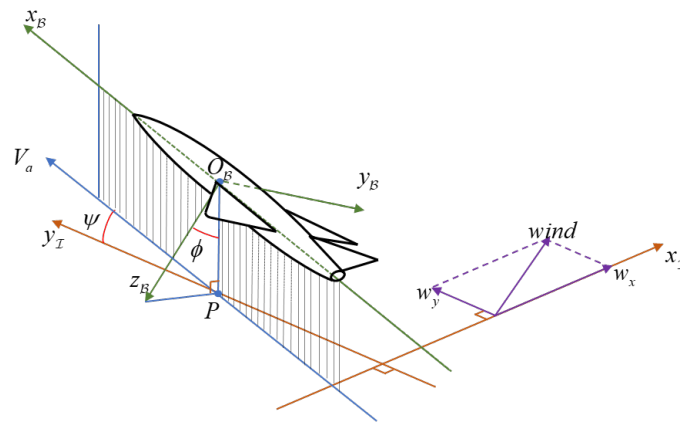

Figure 1. The variables involved in kinematics (1).

In light of the existing modeling result [2], the wind disturbance $d = [w_x, w_y]^\mathrm{T}$ is generated using the exogenous system as follows:

$$
\dot{\omega}_d = A_\omega \omega_d + B_\omega \Delta_\omega(t), \ d = C_\omega \omega_d
\tag{2}
$$

where $\omega_d \in \mathbb{R}^m$ is the state of the exogenous system; $A_\omega \in \mathbb{R}^{m \times m}, B_\omega \in \mathbb{R}_{\geqslant 0}^{m \times n}$ and $C_\omega \in \mathbb{R}_{\geqslant 0}^{2 \times m}$ are the known constant matrices with observable pair (A_ω, C_ω) and natural stable A_ω; $\Delta_\omega(t) \in \mathbb{R}^n$ is the unknown time-varying vector characterizing the modeling uncertainty of the wind disturbance; and m and n are two positive integers, which are the order of the system (2) related to the wind disturbance model established by the user. Regarding the properties of the wind disturbances, there exist oscillatory and damping modes for each direction of the wind disturbance. In the simulation part, we established a fourth-order system to simulate the wind disturbances in two different directions, namely $m = 4$ and $n = 2$.

2.2. Path Following Based on the Serret–Frenet Frame

In terms of the path-following issue, we expect the position of the UAV to follow a prescribed path $l(s) \in \mathbb{R}^2$, which is a smooth curve determined by the length s. To transform the path-following issue into a general control problem, we introduce the Serret–Frenet frame $\mathcal{F}$ to redescribe the kinematic model of the UAV; the Serret–Frenet frame possesses more intuitions than the inertial one $\mathcal{I}$ on representing the positional relationship between the UAV and the prescribed path.

In Figure 2, a schematic diagram is presented to demonstrate the Serret–Frenet frame $\mathcal{F}$, the inertial frame $\mathcal{I}$, and the body frame $\mathcal{B}$, where $P_r(s) = [p_{xr}(s), p_{yr}(s)]^{\mathrm{T}}$ is the projection (reference) point of the UAV on the desired path $l(s)$. The Serret–Frenet frame is defined by the tangent vector $(T_r(s))$ and the normal vector $(N_r(s))$. Then, the coordinate of the UAV in $\mathcal{F}$ is given as $P_F = [0, Y_F]^{\mathrm{T}}$, where Y_F is the vertical distance from the UAV to the reference point. Moreover, χ_r is the desired path angle and θ_r is the rotation angle between $\mathcal{I}$ and $\mathcal{F}$. Thus, we have the following relations [39]:

$$\dot{\chi}_r = \dot{\theta}_r = \omega_c = k\dot{s} \tag{3}$$

where k is the curvature at the reference point $P_r(s)$ of the prescribed path, $\dot{s}$ is the speed of that on the prescribed path, and its specific form will be given later so in (11).
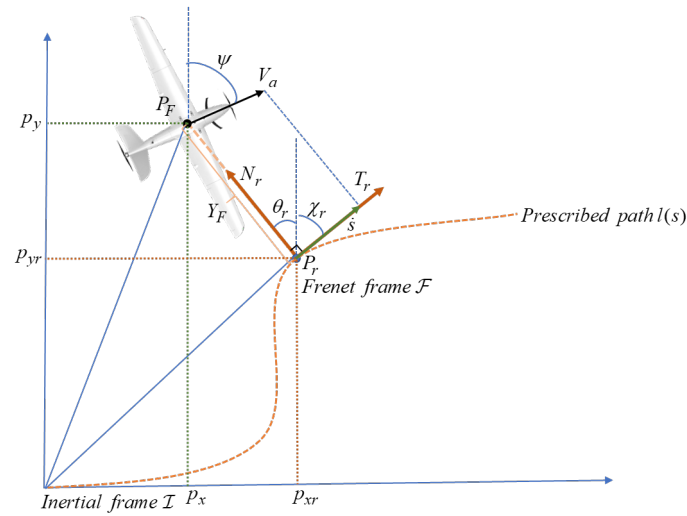

Figure 2. Relationship between $\mathcal{I}$, $\mathcal{F}$, and $\mathcal{B}$.

Based on the above Serret–Frenet Frame, the control objective is transformed to stabilize the distance from the UAV to the prescribed path, i.e., $Y_F \to 0$. According to Figure 2, the coordinate relationship between $\mathcal{I}$ and $\mathcal{F}$ is expressed as

$$P = P_r + R_{\mathcal{F}}^{\mathcal{I}} P_F \tag{4}$$

where $R_{\mathcal{F}}^{\mathcal{I}}$ is the rotation matrix from $\mathcal{F}$ to $\mathcal{I}$, and it has the following form [40]:

$$R_{\mathcal{F}}^{\mathcal{I}} = (R_{\mathcal{I}}^{\mathcal{F}})^{\mathrm{T}} = \begin{bmatrix} \cos\theta_r & -\sin\theta_r \\ \sin\theta_r & \cos\theta_r \end{bmatrix} \tag{5}$$

By using Rodrigues' rotation formula [41], we obtain

$$\frac{d(R_{\mathcal{F}}^{\mathcal{I}} P_F)}{dt} = R_{\mathcal{F}}^{\mathcal{I}} \frac{dP_F}{dt} + R_{\mathcal{F}}^{\mathcal{I}} [\dot{\theta}_r]_\times P_F \tag{6}$$

with $[\dot{\theta}_r]_\times = \begin{bmatrix} 0 & -\dot{\theta}_r \\ \dot{\theta}_r & 0 \end{bmatrix}$.

By invoking (6), the derivative of P in (4) is written as follows: [40]:

$$\begin{aligned} \left(\frac{dP}{dt}\right)_{\mathcal{I}} &= \left(\frac{dP_r}{dt}\right)_{\mathcal{I}} + R_{\mathcal{F}}^{\mathcal{I}} \left(\frac{dP_{\mathcal{F}}}{dt}\right)_{\mathcal{F}} + \left(\frac{dR_{\mathcal{F}}^{\mathcal{I}}}{dt}\right) P_F \\ &= \left(\frac{dP_r}{dt}\right)_{\mathcal{I}} + R_{\mathcal{F}}^{\mathcal{I}} \left(\frac{dP_{\mathcal{F}}}{dt}\right)_{\mathcal{F}} + R_{\mathcal{F}}^{\mathcal{I}} \begin{bmatrix} 0 & -k\dot{s} \\ k\dot{s} & 0 \end{bmatrix} P_F \end{aligned} \tag{7}$$

where $(*)_\mathcal{I}$ and $(*)_\mathcal{F}$ denote the coordinate representation of $*$ in the $\mathcal{I}$ frame and $\mathcal{F}$ frame, respectively.

By multiplying the rotation matrix $R_\mathcal{I}^\mathcal{F}$ on both the left and right sides of (7), we obtain the dynamics of the path-following error P_F in $\mathcal{F}$ as [40].

$$
\begin{aligned}
\dot{P}_F &= R_\mathcal{I}^\mathcal{F}\left(\frac{dP}{dt}\right)_I - R_\mathcal{I}^\mathcal{F}\left(\frac{dP_r}{dt}\right)_I - \begin{bmatrix} 0 & -k\dot{s} \\ k\dot{s} & 0 \end{bmatrix} P_F \\
&= R_\mathcal{B}^\mathcal{F}\begin{bmatrix} V_a \\ 0 \end{bmatrix} + R_\mathcal{I}^\mathcal{F}\begin{bmatrix} w_x \\ w_y \end{bmatrix} - R_\mathcal{I}^\mathcal{F}\left(\frac{dP_r}{dt}\right)_I - \begin{bmatrix} 0 & -k\dot{s} \\ k\dot{s} & 0 \end{bmatrix} P_F
\end{aligned}
\tag{8}
$$

where $R_\mathcal{B}^\mathcal{F}$ is the rotation matrix from $\mathcal{B}$ to $\mathcal{F}$ as [40].

$$
R_\mathcal{B}^\mathcal{F} = (R_\mathcal{F}^\mathcal{B})^\mathrm{T} = \begin{bmatrix} \cos\psi_e & -\sin\psi_e \\ \sin\psi_e & \cos\psi_e \end{bmatrix}
\tag{9}
$$

with $\psi_e = \psi - \chi_r$.

Finally, by expanding (8) and integrating (1), the dynamics of the path-following error in $\mathcal{F}$ is shown as

$$
\begin{cases}
\dot{Y}_F = V_a\sin\psi_e - \sin\theta_r w_x + \cos\theta_r w_y \\
\dot{\psi}_e = \dot{\psi} - \dot{\chi}_r = \frac{g}{V_a}\tan\phi - k\dot{s} \\
\dot{\phi} = b_\phi(u - \phi)
\end{cases}
\tag{10}
$$

and now, $\dot{s}$ denotes the moving speed of the reference point P_r on the desired path, with the following form [40]:

$$
\dot{s} = V_a\cos\psi_e/(1 - kY_F)
\tag{11}
$$

2.3. Control Objective

With the path-following error dynamics (10), the control objective of this work is transformed to stabilize Y_F by designing the control law for u.

To proceed with the control development, the following assumptions are made:

Assumption 1 ([38]). *For the time-varying vector $\Delta_\omega(t) \in \mathbb{R}^n$ in the exogenous system (2), there exists a known constant vector $\bar{\Delta}_\omega \geqslant 0_{n\times 1}$ satisfying $|\Delta_\omega(t)|^* \leqslant \bar{\Delta}_\omega$;*

Assumption 2 ([42]). *Assume that $|\psi - \chi_r|$ is less than $\frac{\pi}{2}$, $|\psi_e| < \frac{\pi}{2}$, which means $\psi_e = \psi_e^*$ when $\sin\psi_e = \sin\psi_e^*$ for any $|\psi_e^*| < \frac{\pi}{2}$;*

Assumption 3 ([43]). *The rolling angle of the UAV is less than $\frac{\pi}{2}$, i.e., $|\phi| < \frac{\pi}{2}$, which indicates $\phi = \phi^*$ when $\tan\phi = \tan\phi^*$ for any $|\phi^*| < \frac{\pi}{2}$;*

Assumption 4 ([42]). *The infinite norm of wind d is less than UAV's actual airspeed V_a, which indicates $||d|| < V_a$ for all $t \geqslant 0$.*

Remark 1. *The wind disturbance induced on the UAV should be bounded, and accordingly, for the states of the exogenous system. Moreover, there are abundant modeling results [2] based on the wind data to make A_ω accurate. All these data make sure the boundedness of the modeling uncertainty $\Delta_\omega(t)$ and then the reasonability of Assumption 1.*

Remark 2. *The heading angle of the UAV is defined in $(-\pi, \pi]$. The objective of path following is that the nose of the UAV adjusts to the desired orientation as quickly as possible. Therefore, the error of the course angle or heading angle is defined in $[0, \pi]$. The error can be converted to $[-\pi/2, \pi/2]$ by selecting a reasonable origin. Then, it is clear that Assumption 2 is rational.*

Remark 3. *In this work, we concentrate on the path-following control of the UAV. Of course, the normal flight situation of the UAV can accomplish the path-following objective. Thus, we only consider the normal flight situations of the UAV that do not include upside-down flying. Specifically, the roll angle of the UAV is within the range of $[-\pi/2, \pi/2]$, which indicates Assumption 3 is reasonable.*

Remark 4. *Assumption 4 means that the wind resistance of the UAV is capable of being improved through controller design, while it is constrained by the physical performance of the UAV.*

At the same time, for the design and use of DIOB, the following two lemmas are given:

Lemma 1 ([44]). *For any given constant $\epsilon_M > 0$ and time-varying signal ϑ_M, the inequality $0 \leqslant |\vartheta_M| - \vartheta_M \tanh(\frac{\vartheta_M}{\epsilon_M}) \leqslant c_M \epsilon_M$ always holds with $c_M = \exp(-c_M - 1) = 0.2785$.*

Lemma 2 (Positive system, [45]). *Suppose that there is a Metzler matrix $K_M \in \mathbb{R}^{m \times m}$(i.e., all its non-diagonal elements are non-negative.) and a non-negative time-varying vector $\Delta_M(t) \in \mathbb{R}^m_{\geqslant 0}$, so that the system $\dot{h}_M = K_M h_M + \Delta_M(t)$ has a unique solution for any initial state $h_M(0) \in \mathbb{R}^m$. Then, given any initial state $h_M(0) \in \mathbb{R}^m_{\geqslant 0}$, it satisfies $h_M(t) \in \mathbb{R}^m_{\geqslant 0}$ for any $t > 0$.*

3. Control Design and Stability Analysis

In this section, the DIOB is designed for the UAV kinematics in the inertial frame. The path-following control design is then presented based on the dynamic surface control technique and the auxiliary system is adopted to deal with the command limitation. Lastly, the stability analysis of the closed-loop system is presented.

3.1. Disturbance Interval Observer Design

In order to suppress the influence of wind disturbance on the UAV, a DIOB is introduced in this work. It will realize the interval estimation of the wind disturbance based on the nominal kinematics of the UAV in (1) and the known dynamics of the wind disturbance in (2).

For the simplicity of denotation, the position kinematics of the UAV in (1) is rewritten in the following vector form:

$$\dot{x}_p = f(\cdot) + d \tag{12}$$

with $x_p = [p_x, p_y]^{\mathrm{T}}$ and $f(\cdot) = V_a[\sin \psi, \cos \psi]^{\mathrm{T}}$.

With the observer gain matrix $L_\omega \in \mathbb{R}^{m \times 2}$ and the positive definite coordinate transformation matrix $P_\omega \in R^{m \times m}$, define intermediate variable $z_\omega = P_\omega(\omega_d - L_\omega l_\omega(x_p))$ and the function vector $l_\omega(x_p) = [-p_x, -p_y]^{\mathrm{T}}$. By invoking (2) and (12), the dynamics of the intermediate variable z_ω is obtained as follows [2]:

$$\dot{z}_\omega = P_\omega(A_\omega - L_\omega C_\omega)Q_\omega z_\omega + \Theta_\omega + P_\omega B_\omega \Delta_\omega(t) \tag{13}$$

where Q_ω is the inverse matrix of P_ω, and they constitute the coordinate transformation for $(A_\omega - L_\omega C_\omega)$, Θ_ω is a known function vector with the following form:

$$\Theta_\omega = P_\omega(A_\omega - L_\omega C_\omega)L_\omega l_\omega(x_p) - P_\omega L_\omega \frac{\partial l_\omega(x_p)}{\partial x_p^{\mathrm{T}}} f(\cdot)$$

Then, the interval observer is designed for the intermediate variable z_ω, and the specific form of the DIOB is given by [2]

$$\begin{cases} \dot{\hat{z}}_u = \Gamma_\omega \hat{z}_u + \Theta_\omega + |P_\omega|^* B_\omega \bar{\Delta}_\omega \\ \dot{\hat{z}}_l = \Gamma_\omega \hat{z}_l + \Theta_\omega - |P_\omega|^* B_\omega \bar{\Delta}_\omega \\ \hat{d}_u = C_\omega \left(Q_\omega^+ \hat{z}_u - Q_\omega^- \hat{z}_l + L_\omega l_\omega(x_p) \right) \\ \hat{d}_l = C_\omega \left(Q_\omega^+ \hat{z}_l - Q_\omega^- \hat{z}_u + L_\omega l_\omega(x_p) \right) \end{cases} \quad (14)$$

where $\Gamma_\omega = P_\omega (A_\omega - L_\omega C_\omega) Q_\omega$, $\hat{z}_u, \hat{z}_l \in \mathbb{R}^m$ are the internal states of the DIOB and they constitute the interval estimate of the intermediate variable z_ω, $\hat{d}_u, \hat{d}_l \in \mathbb{R}^2$ are the outputs of the DIOB and they constitute the interval estimate of the wind disturbance d, and $\bar{\Delta}_\omega$ is given in Assumption 1.

Define the estimation errors of the intermediate variable z_ω as

$$\tilde{z}_u = \hat{z}_u - z_\omega, \ \tilde{z}_l = z_\omega - \hat{z}_l$$

and the variables of the wind disturbance d as

$$\tilde{d}_u = \hat{d}_u - d, \ \tilde{d}_l = d - \hat{d}_l$$

Then, we have the following lemma that summarizes the design condition of the DIOB:

Lemma 3 (DIOB, [38]). *For the UAV kinematic model* (1) *under the unknown wind disturbance generated by* (2), *design the DIOB according to* (14):

- *If the designed matrices L_ω and P_ω make Γ_ω be simultaneously Metzler and Hurwitz;*
- *If the initial conditions of $\hat{z}_u$ and $\hat{z}_l$ satisfy $\hat{z}_l(0) \leqslant z_\omega(0) \leqslant \hat{z}_u(0)$.*

Then, the estimation errors $\tilde{d}_l$ and $\tilde{d}_u$ of the DIOB are non-negative and bounded.

Proof of Lemma 3. By considering (13) and (14), the estimation errors $\tilde{z}_u$ and $\tilde{z}_l$ of intermediate variable z_ω satisfy the following differential equations:

$$\begin{cases} \dot{\tilde{z}}_u = \Gamma_\omega \tilde{z}_u + |P_\omega|^* B_\omega \bar{\Delta}_\omega - P_\omega B_\omega \Delta_\omega(t) \\ \dot{\tilde{z}}_l = \Gamma_\omega \tilde{z}_l + |P_\omega|^* B_\omega \bar{\Delta}_\omega + P_\omega B_\omega \Delta_\omega(t) \end{cases} \quad (15)$$

According to the definition of B_ω in (2), we know it satisfies $B_\omega \geqslant 0_{m \times n}$. According to Assumption 1, we further have $-|P_\omega|^* B_\omega \bar{\Delta}_\omega \leqslant P_\omega B_\omega \Delta_\omega(t) \leqslant |P_\omega|^* B_\omega \bar{\Delta}_\omega$. Based on Lemma 2, the design condition of Metzler matrix Γ_ω, and the initial condition of $\hat{z}_l(0) \leqslant z_\omega(0) \leqslant \hat{z}_u(0)$, it is found that $\tilde{z}_u$ and $\tilde{z}_l$ are non-negative.

Define the interval width vector $s_\omega = \tilde{z}_u + \tilde{z}_l$ for the intermediate variable z_w. Since Γ_ω is designed to be a Hurwitz matrix, there must be another matrix $R_\omega \succ 0$ such that $R_\omega \Gamma_\omega + \Gamma_\omega^{\mathrm{T}} R_\omega \prec 0$. Define the Lyapunov function $\mathcal{V}_\omega = s_\omega^{\mathrm{T}} R_\omega s_\omega$. By considering (15), it is found that the derivative of $\mathcal{V}_\omega$ satisfies the following inequality:

$$\begin{aligned} \dot{\mathcal{V}}_\omega &= s_\omega^{\mathrm{T}} R_\omega (\dot{\tilde{z}}_u + \dot{\tilde{z}}_l) + (\dot{\tilde{z}}_u + \dot{\tilde{z}}_l)^{\mathrm{T}} R_\omega s_\omega \\ &= s_\omega^{\mathrm{T}} R_\omega (\Gamma_\omega \tilde{z}_u + \Gamma_\omega \tilde{z}_l + 2|P_\omega|^* B_\omega \bar{\Delta}_\omega) + (\Gamma_\omega \tilde{z}_u + \Gamma_\omega \tilde{z}_l + 2|P_\omega|^* B_\omega \bar{\Delta}_\omega)^{\mathrm{T}} R_\omega s_\omega \\ &= s_\omega^{\mathrm{T}} R_\omega \Gamma_\omega s_\omega + s_\omega^{\mathrm{T}} \Gamma_\omega^{\mathrm{T}} R_\omega s_\omega + 2 s_\omega^{\mathrm{T}} R_\omega (|P_\omega|^* B_\omega \bar{\Delta}_\omega) + 2(|P_\omega|^* B_\omega \bar{\Delta}_\omega)^{\mathrm{T}} R_\omega s_\omega \\ &\leqslant s_\omega^{\mathrm{T}} (R_\omega \Gamma_\omega + \Gamma_\omega^{\mathrm{T}} R_\omega + 2\eta_\omega R_\omega R_\omega) s_\omega + \left\| |P_\omega|^* B_\omega \bar{\Delta}_\omega \right\|^2 / \eta_\omega \end{aligned} \quad (16)$$

where $\eta_\omega > 0$ is an adjustable parameter. It is known from $R_\omega \Gamma_\omega + \Gamma_\omega^{\mathrm{T}} R_\omega \prec 0$ that there must be a suitable η_ω to make $R_\omega \Gamma_\omega + \Gamma_\omega^{\mathrm{T}} R_\omega + 2\eta_\omega R_\omega R_\omega \prec 0$ which indicates that the interval width vector s_ω is bounded. Furthermore, because of the non-negative characteristics of $\tilde{z}_u$ and $\tilde{z}_l$, we obtain that $\tilde{z}_u$ and $\tilde{z}_l$ are also bounded.

Consider the definitions of estimation errors $\tilde{d}_u$ and $\tilde{d}_l$, and they satisfy the following equations:

$$\tilde{d}_u = \hat{d}_u - d = C_\omega(Q_\omega^+ \tilde{z}_u + Q_\omega^- \tilde{z}_l), \ \tilde{d}_l = d - \hat{d}_l = C_\omega(Q_\omega^+ \tilde{z}_l + Q_\omega^- \tilde{z}_u) \tag{17}$$

Finally, we can conclude that $\tilde{d}_l$ and $\tilde{d}_u$ are non-negative and bounded. This completes the proof. $\square$

3.2. Robust Constrained Control Design

At this stage, the robust constrained control law is designed for the path-following error dynamics (10). Before presenting the control design, a block diagram of the closed-loop system is shown in Figure 3. It is seen from Figure 3 that the block "UAV" is the actual plant. The block "Serret–Frenet transformation" is used to calculate the path-following error in the Serret–Frenet frame. The block "DIOB" generates wind disturbance estimation for "Virtual Control Law 1". The designed control follows the dynamic surface technique. Specifically, two virtual control laws, i.e., "Virtual Control Law 1" and "Virtual Control Law 2", and a control law, i.e., "actual control law", are designed. In order to avoid the differential explosion issue, two filters, i.e., "Filter 1" and "Filter 2", are introduced to obtain the deviations of the virtual control laws. Moreover, the "auxiliary system" is employed to solve the instability problem caused by "command limitation".
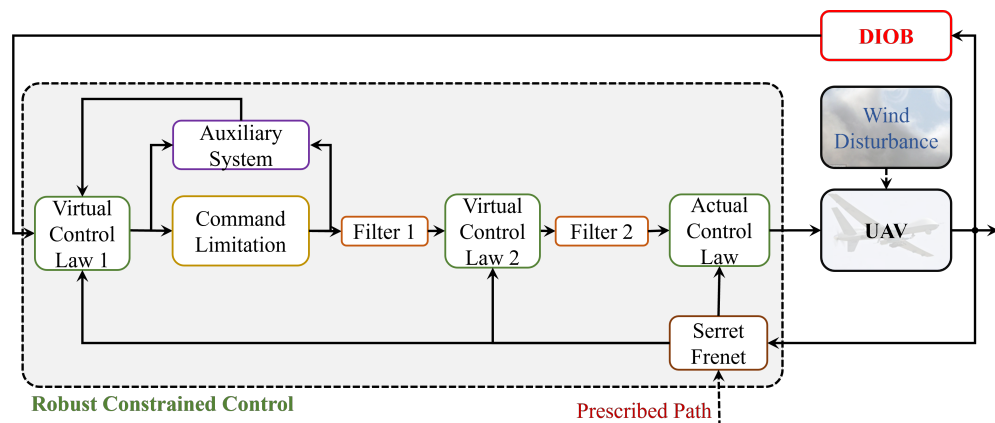

Figure 3. Structure of the closed-loop system.

The control design follows a step-by-step procedure.

Step 1: For the convenience of symbol use, let

$$[\hat{w}_x, \hat{w}_y]^{\mathrm{T}} = \hat{d} = 0.5(\hat{d}_u + \hat{d}_l), \ [\overline{w}_x, \overline{w}_y]^{\mathrm{T}} = \overline{d} = 0.5(\hat{d}_u - \hat{d}_l)$$

represent the middle-value vector and the weight vector of the DIOB, respectively. In the controller design process, we use $\hat{d}$ and $\overline{d}$ as the compensation and robust terms, respectively.

Define path-following error $e_Y = Y_F$. According to the controller design goal, i.e., $e_Y \to 0$, we design a positive definite function about e_Y to measure the energy of the system tracking error. According to the general Lyapunov function design method, we select the following positive definite quadratic function:

$$\mathcal{V}_0 = \frac{1}{2} k_1 e_Y^2 \tag{18}$$

where $k_1 > 0$ is a tuning parameter to be designed.

By considering the path-following error dynamics (10), the differential form of $\mathcal{V}_0$ is written as

$$\dot{\mathcal{V}}_0 = k_1 e_Y (V_a \sin \psi_e - \sin \theta_r w_x + \cos \theta_r w_y) \tag{19}$$

To overcome the non-affine non-linearity of $\sin(\cdot)$, we directly design the virtual control law $x_1^d \in [-1, 1]$ for "$\sin \psi_e$". In light of the natural bounded characteristic of $\sin(\cdot)$, the virtual control law x_1^d undergoes the following command limitation:

$$x_1^d = \begin{cases} (\gamma \tau + (1 - \gamma) \tau \tanh \frac{|x_1^c|/\tau - \gamma}{1 - \gamma}) \mathrm{sign}(x_1^c) & |x_1^c| > \gamma \tau \\ x_1^c & |x_1^c| \leqslant \gamma \tau \end{cases} \tag{20}$$

where x_1^c is the nominally designed virtual control law of "$\sin \psi_e$" without considering the command limitation, and $0 < \gamma < 1$ and $\tau > 0$ are the adjustable parameter and the amplitude of limitation, respectively.

In order to avoid the instability of the control system caused by the command limitation (20), an auxiliary system is constructed as [46]

$$\dot{\sigma}_{x1} = \begin{cases} -k_\sigma \sigma_{x1} - \frac{1}{\sigma_{x1}} (|k_1 V_a e_Y \Delta x_1| + \frac{\Delta x_1^2}{2}) + \Delta x_1 & |\sigma_{x1}| > \mu \\ 0 & |\sigma_{x1}| \leqslant \mu \end{cases} \tag{21}$$

where $\Delta x_1 = x_1^c - x_1^d$, $\sigma_{x1} \in \mathbb{R}$ is the state of the auxiliary system, $k_\sigma > 0$ is the parameter to be designed, and μ is a positive tuning number which should be appropriately selected according to the system performance requirement.

Then, design the virtual control law x_1^c as follows:

$$\begin{aligned} x_1^c = & - \left(\frac{c_1 e_Y}{V_a} + \frac{\bar{w}_x \sin \theta_r e_Y}{V_a} \tanh \left(\frac{\sin \theta_r e_Y}{\epsilon_1} \right) + \frac{\bar{w}_y \cos \theta_r e_Y}{V_a} \tanh \left(\frac{\cos \theta_r e_Y}{\epsilon_1} \right) \right) \\ & + \frac{\hat{w}_x \sin \theta_r - \hat{w}_y \cos \theta_r}{V_a} - \sigma_{x1} \end{aligned} \tag{22}$$

where $c_1 > 0$ is the feedback gain and $\epsilon_1 > 0$ is a tuning parameter.

Meanwhile, in order to avoid the complexity explosion problem, a filter variable $x_2^f \in \mathbb{R}$ is introduced. The form of the low-pass filter is given as follows [47]:

$$\omega_1 \dot{x}_2^f + x_2^f = x_1^d, \ x_2^f(0) = x_1^d(0) \tag{23}$$

where $\omega_1 > 0$ is the time constant of the filter to be designed.

Define the tracking error $e_2 = \sin \psi_e - x_2^f$ for $\sin \psi_e$ and the estimation error of the low-pass filter as

$$\delta_1 = x_2^f - x_1^d \tag{24}$$

Substituting (22) and (23) into (19) yields

$$\begin{aligned} \dot{\mathcal{V}}_0 = & k_1 e_Y (V_a (e_2 + x_2^f) - \sin \theta_r w_x + \cos \theta_r w_y) \\ = & k_1 e_Y (V_a (e_2 + x_1^d + \delta_1) - \sin \theta_r w_x + \cos \theta_r w_y) \\ = & k_1 e_Y (V_a (e_2 - \Delta x_1 + x_1^c + \delta_1) - \sin \theta_r w_x + \cos \theta_r w_y) \\ = & -c_1 k_1 e_Y^2 + k_1 V_a e_Y (e_2 + \delta_1) - k_1 e_Y \sin \theta_r \tilde{w}_x + k_1 e_Y \cos \theta_r \tilde{w}_y \\ & - k_1 e_Y \sin \theta_r \tanh(\sin \theta_r e_Y / \epsilon_1) \bar{w}_x - k_1 \cos \theta_r e_Y \tanh(\cos \theta_r e_Y / \epsilon_1) \bar{w}_y \\ & - k_1 V_a e_Y \Delta x_1 - k_1 V_a e_Y \sigma_{x1} \end{aligned} \tag{25}$$

where $[\bar{w}_x, \bar{w}_y]^{\mathrm{T}} = \tilde{d} = d - \hat{d} = [\hat{w}_x - w_x, \hat{w}_y - w_y]^{\mathrm{T}}$.

According to the interval property of the DIOB in Lemma 3, we have

$$\tilde{d}_u = \hat{d}_u - d \geqslant 0, \; \tilde{d}_l = d - \hat{d}_l \geqslant 0$$

and then,

$$\bar{d} - \tilde{d} = 0.5(\hat{d}_u - \hat{d}_l) - (d - 0.5(\hat{d}_u + \hat{d}_l)) = \hat{d}_u - d \geqslant 0$$
$$\bar{d} + \tilde{d} = 0.5(\hat{d}_u - \hat{d}_l) + (d - 0.5(\hat{d}_u + \hat{d}_l)) = d - \hat{d}_l \geqslant 0$$

which indicates $\bar{d} \geqslant |\tilde{d}|$, namely,

$$|\tilde{w}_x| \leqslant \bar{w}_x, |\tilde{w}_y| \leqslant \bar{w}_y \tag{26}$$

In light of Lemma 1, we further have

$$\begin{cases} |e_\Upsilon \sin\theta_r \tilde{w}_x| \leqslant |\sin\theta_r e_\Upsilon \tilde{w}_x| \leqslant \sin\theta_r e_\Upsilon \tanh(\sin\theta_r e_\Upsilon / \epsilon_1)\bar{w}_x + \epsilon_1 \bar{w}_x \\ |e_\Upsilon \cos\theta_r \tilde{w}_y| \leqslant |\cos\theta_r e_\Upsilon \tilde{w}_y| \leqslant \cos\theta_r e_\Upsilon \tanh(\cos\theta_r e_\Upsilon / \epsilon_1)\bar{w}_y + \epsilon_1 \bar{w}_y \end{cases} \tag{27}$$

By considering (25) and (27), we have

$$\begin{aligned} \dot{\mathcal{V}}_0 \leqslant & - c_1 k_1 e_\Upsilon^2 + k_1 V_a e_\Upsilon(e_2 + \delta_1) + k_1 |e_\Upsilon \sin\theta_r \tilde{w}_x| - k_1 V_a e_\Upsilon \Delta x_1 - k_1 V_a e_\Upsilon \sigma_{x1} \\ & - k_1 \sin\theta_r e_\Upsilon \tanh\left(\frac{sin\theta_r e_\Upsilon}{\epsilon_1}\right)\bar{w}_x + k_1 |e_\Upsilon \cos\theta_r \tilde{w}_y| - k_1 \cos\theta_r e_\Upsilon \tanh\left(\frac{\cos\theta_r e_\Upsilon}{\epsilon_1}\right)\bar{w}_y \\ \leqslant & - c_1 k_1 e_\Upsilon^2 + k_1 V_a e_\Upsilon(e_2 + \delta_1) + k_1 \epsilon_1 \bar{w}_x + k_1 \epsilon_1 \bar{w}_y - k_1 V_a e_\Upsilon \Delta x_1 - k_1 V_a e_\Upsilon \sigma_{x1} \end{aligned} \tag{28}$$

Define the positive function $\mathcal{V}_1$ as

$$\mathcal{V}_1 = \mathcal{V}_0 + \frac{1}{2}\sigma_{x1}^2 = \frac{1}{2}k_1 e_\Upsilon^2 + \frac{1}{2}\sigma_{x1}^2 \tag{29}$$

Considering the situation when saturation occurs, and invoking (18) and (28), we have the derivative form of $\mathcal{V}_1$ as follows:

$$\begin{aligned} \dot{\mathcal{V}}_1 \leqslant & - c_1 k_1 e_\Upsilon^2 + k_1 V_a e_\Upsilon(e_2 + \delta_1) + k_1 \epsilon_1 \bar{w}_x + k_1 \epsilon_1 \bar{w}_y - k_1 V_a e_\Upsilon \Delta x_1 - k_1 V_a e_\Upsilon \sigma_{x1} \\ & + \sigma_{x1}(-k_\sigma \sigma_{x1} - \frac{1}{\sigma_{x1}}(|k_1 V_a e_\Upsilon \Delta x_1| + \frac{\Delta x_1^2}{2}) + \Delta x_1) \\ = & - c_1 k_1 e_\Upsilon^2 + k_1 V_a e_\Upsilon(e_2 + \delta_1) + k_1 \epsilon_1 \bar{w}_x + k_1 \epsilon_1 \bar{w}_y - k_1 V_a e_\Upsilon \Delta x_1 - k_1 V_a e_\Upsilon \sigma_{x1} \\ & - k_\sigma \sigma_{x1}^2 - |k_1 V_a e_\Upsilon \Delta x_1| - \frac{\Delta x_1^2}{2} + \sigma_{x1}\Delta x_1 \end{aligned} \tag{30}$$

By using Young's inequality, we have

$$\sigma_{x1}\Delta x_1 \leqslant \frac{1}{2}\sigma_{x1}^2 + \frac{1}{2}\Delta x_1^2 \tag{31}$$

With further consideration of (30) and (31), we obtain

$$\begin{aligned} \dot{\mathcal{V}}_1 \leqslant & - c_1 k_1 e_\Upsilon^2 + k_1 V_a e_\Upsilon(e_2 + \delta_1) + k_1 \epsilon_1 \bar{w}_x + k_1 \epsilon_1 \bar{w}_y - k_1 V_a e_\Upsilon \Delta x_1 - k_1 V_a e_\Upsilon \sigma_{x1} \\ & - k_\sigma \sigma_{x1}^2 - |k_1 V_a e_\Upsilon \Delta x_1| + \frac{\sigma_{x1}^2}{2} \end{aligned} \tag{32}$$

Because of $-k_1 V_a e_\Upsilon \Delta x_1 - |k_1 V_a e_\Upsilon \Delta x_1| \leqslant 0$, we can reduce inequality (32) as

$$\dot{\mathcal{V}}_1 \leqslant - c_1 k_1 e_\Upsilon^2 + k_1 V_a e_\Upsilon(e_2 + \delta_1) + k_1 \epsilon_1 (\bar{w}_x + \bar{w}_y) - k_1 V_a e_\Upsilon \sigma_{x1} + (\frac{1}{2} - k_\sigma)\sigma_{x1}^2 \tag{33}$$

Considering the situation when saturation does not occur, the state of the auxiliary system satisfies $\sigma_{x1} = 0$. We have the derivative form of $\mathcal{V}_1$ as follows:

$$\dot{\mathcal{V}}_1 \leqslant - c_1 k_1 e_Y^2 + k_1 V_a e_Y (e_2 + \delta_1) + k_1 \epsilon_1 \bar{w}_x + k_1 \epsilon_1 \bar{w}_y \tag{34}$$

Step 2: Define a Lyapunov function candidate $\mathcal{V}_2$ as

$$\mathcal{V}_2 = \frac{1}{2} k_2 e_2^2 \tag{35}$$

where $k_2 > 0$ is an adjustable parameter.

To design the next virtual control law, the differential form of $\mathcal{V}_2$ is written as

$$\dot{\mathcal{V}}_2 = k_2 e_2 (\cos \psi_e \dot{\psi}_e + \frac{\delta_1}{\omega_1}) \tag{36}$$

By invoking (10), we obtain

$$\dot{\mathcal{V}}_2 = k_2 e_2 \left(\cos \psi_e (\frac{g}{V_a} \tan \phi - k\dot{s}) + \frac{\delta_1}{\omega_1} \right) \tag{37}$$

Then, we design the virtual control law for "$\tan \phi$" as

$$x_2^d = \frac{V_a k\dot{s}}{g} - \frac{V_a (c_2 e_2 + \frac{k_1}{k_2} V_a e_Y)}{g \cos \psi_e} \tag{38}$$

where $c_2 > 0$ is the feedback gain, and $\cos \psi_e$ is always positive under Assumption 2.

Process x_2^d in the same way as x_1^d and design low-pass filter as [47]

$$\omega_2 \dot{x}_3^f + x_3^f = x_2^d, \ x_3^f(0) = x_2^d(0) \tag{39}$$

where $x_3^f \in \mathbb{R}$ is the filter variable, and $\omega_2 > 0$ is the time constant of the filter. Accordingly, the estimation error of the low-pass filter (39) is defined as

$$\delta_2 = x_3^f - x_2^d \tag{40}$$

According to Assumption 3, define tracking error of virtual control law as $e_3 = \tan \phi - x_3^f$. By using (38), the derivative of $\mathcal{V}_2$ is rewritten as

$$\dot{\mathcal{V}}_2 = k_2 e_2 \left(\cos \psi_e (\frac{g}{V_a} (e_3 + x_3^f) - k\dot{s}) + \frac{\delta_1}{\omega_1} \right) \tag{41}$$

By using (40), we obtain the following derivative form of $\mathcal{V}_2$:

$$\begin{aligned}
\dot{\mathcal{V}}_2 &= k_2 e_2 \left(\cos \psi_e (\frac{g}{V_a} (e_3 + x_2^d + \delta_2) - k\dot{s}) + \frac{\delta_1}{\omega_1} \right) \\
&= - c_2 k_2 e_2^2 + k_2 e_2 \cos \psi_e \frac{g}{V_a} \delta_2 + k_2 e_2 e_3 \cos \psi_e \frac{g}{V_a} + k_2 e_2 \frac{\delta_1}{\omega_1} - k_1 V_a e_Y e_2
\end{aligned} \tag{42}$$

Step 3: Choose another Lyapunov function candidate $\mathcal{V}_3$ as

$$\mathcal{V}_3 = \frac{1}{2} k_3 e_3^2 \tag{43}$$

where $k_3 > 0$ is an adjustable parameter.

By invoking (10), the differential from of $\mathcal{V}_3$ is shown as

$$\dot{\mathcal{V}}_3 = k_3 e_3 (\dot{\phi} \sec^2 \phi - \dot{x}_3^f) \tag{44}$$

Using (39), we have the following inequality:

$$\dot{V}_3 = k_3 e_3 \left((\sec^2 \phi) b_\phi (u - \phi) + \frac{\delta_2}{\omega_2} \right) \tag{45}$$

Thus, we design the nominal control law u as

$$u = \phi + \frac{\cos^2 \phi}{b_\phi} \left(-c_3 e_3 - \frac{k_2}{k_3} e_2 \cos \psi_e \frac{g}{V_a} \right) \tag{46}$$

where $c_3 > 0$ is the feedback gain.

Substituting the control law (46) into (45) yields

$$\dot{V}_3 = -c_3 k_3 e_3^2 + k_3 e_3 \frac{\delta_2}{\omega_2} - k_2 e_2 e_3 \cos \psi_e \frac{g}{V_a} \tag{47}$$

3.3. Stability Analysis

Theorem 1. *For the kinematics model (1) of the UAV, consider the wind disturbance is generated by using (2). Design the DIOB according to Lemma 3. Based on the filter (23), (39), and the auxiliary system (21), design the virtual control law (22) and (38), and control law (46) for the path-following error dynamics (10). With any given parameters γ, τ, μ, η_ω, and η_ϵ, if the matrices R_ω, P_ω, Q_ω, L_ω, the feedback gains c_1, c_2, c_3, filters' parameters ω_1, ω_2, and the tuning parameters k_1, k_2, k_3, k_σ satisfy the following linear matrix inequalities:*

$$\begin{cases} \Xi_C \prec 0 \\ \Xi_D \prec 0 \end{cases} \tag{48}$$

where Ξ_C and Ξ_D have the following forms:

$$\Xi_C = \begin{bmatrix} -c_1 k_1 & 0_{1\times1} & 0_{1\times1} & k_1 V_a/2 & 0_{1\times1} & -0.5 k_1 V_a \\ 0_{1\times1} & -c_2 k_2 & 0_{1\times1} & k_2/(2\omega_1) & k_2 g/(2V_a) & 0_{1\times1} \\ 0_{1\times1} & 0_{1\times1} & -c_3 k_3 & k_3/(2\omega_2) & 0_{1\times1} & 0_{1\times1} \\ k_1 V_a/2 & k_2/(2\omega_1) & k_3/(2\omega_2) & -1/\omega_1 & 0_{1\times1} & 0_{1\times1} \\ 0_{1\times1} & k_2 g/(2V_a) & 0_{1\times1} & 0_{1\times1} & -1/\omega_2 & 0_{1\times1} \\ -0.5 k_1 V_a & 0_{1\times1} & 0_{1\times1} & 0_{1\times1} & 0_{1\times1} & 0.5 - k_\sigma \end{bmatrix}$$

$$\Xi_D = \begin{bmatrix} R_\omega \Gamma_\omega + \Gamma_\omega^T R_\omega + \eta_\epsilon I_m & * & * \\ R_\omega & -0.5/\eta_\omega & * \\ \Lambda & 0_{1\times1} & -1/(k_1 \epsilon_1 \eta_\epsilon) \end{bmatrix}$$

with $\Lambda = [1,1] C_\omega |Q_\omega|^*$, then the UAV can stably follow the prescribed path.

Proof of Theorem 1. Firstly, we analyze the error of the low-pass filter contained in (23). From (20) and (22), we know that there exists a constant $\bar{x}_1^d > 0$ such that $|\dot{x}_1^d| \leqslant \bar{x}_1^d$. By using (23) and (24), we obtain

$$\dot{\delta}_1 = \dot{x}_2^f - \dot{x}_1^d = \frac{x_1^d - x_2^f}{\omega_1} - \dot{x}_1^d = -\frac{1}{\omega_1} \delta_1 - \dot{x}_1^d \leqslant -\frac{1}{\omega_1} \delta_1 + \bar{x}_1^d \tag{49}$$

By solving the differential equation, we have

$$\delta_1 \leqslant (\delta_1(0) - \omega_1 \bar{x}_1^d) e^{-\frac{t}{\omega}} + \omega_1 \bar{x}_1^d \tag{50}$$

Obviously, there is a constant $\bar{\delta}_1 > 0$ that makes $|\delta_1| \leqslant \bar{\delta}_1$. Similarly, there are constants $\bar{\delta}_2 > 0$ and $\bar{x}_2^d > 0$ that makes $|\delta_2| \leqslant \bar{\delta}_2$ and $|\dot{x}_2^d| \leqslant \bar{x}_2^d$.

Define a positive function as

$$
\begin{aligned}
\mathcal{V}_4 =& \mathcal{V}_1 + \mathcal{V}_2 + \mathcal{V}_3 + \mathcal{V}_\omega + 0.5\delta_1^2 + 0.5\delta_2^2 \\
=& 0.5k_1 e_Y^2 + 0.5k_2 e_2^2 + 0.5k_3 e_3^2 + 0.5\delta_1^2 + 0.5\delta_2^2 + s_\omega^{\mathrm{T}} R_\omega s_\omega + 0.5\sigma_{x1}^2
\end{aligned}
\tag{51}
$$

By using (16), (33), (42), and (47), we have the following derivative form of $\mathcal{V}_4$:

$$
\begin{aligned}
\dot{\mathcal{V}}_4 =& \dot{\mathcal{V}}_1 + \dot{\mathcal{V}}_2 + \dot{\mathcal{V}}_3 + \dot{\mathcal{V}}_\omega + \delta_1 \dot{\delta}_1 + \delta_2 \dot{\delta}_2 \\
\leqslant& -c_1 k_1 e_Y^2 - c_2 k_2 e_2^2 - c_3 k_3 e_3^2 + k_1 V_a e_Y \delta_1 + k_2 \frac{g}{V_a} e_2 \delta_2 + \frac{k_2}{\omega_1} e_2 \delta_1 + (\frac{1}{2} - k_\sigma)\sigma_{x1}^2 \\
& + \frac{k_3}{\omega_2} e_3 \delta_2 + k_1 \epsilon_1 (\bar{w}_x + \bar{w}_y) - \frac{\delta_1^2}{\omega_1} + \bar{\delta}_1 \bar{x}_1^d - \frac{\delta_2^2}{\omega_2} + \bar{\delta}_2 \bar{x}_2^d - k_1 V_a e_Y \sigma_{x1} \\
& + s_\omega^{\mathrm{T}} (R_\omega \Gamma_\omega + \Gamma_\omega^{\mathrm{T}} R_\omega + 2\eta_\omega R_\omega R_\omega)s_\omega + \left\||P_\omega|^* B_\omega \bar{\Delta}_\omega\right\|^2 / \eta_\omega
\end{aligned}
\tag{52}
$$

After combining the DIOB in (17), we obtain $\bar{w}_x + \bar{w}_y = [1,1]\bar{d} = [1,1]C_\omega |Q_\omega|^* s_\omega$. The inequality (52) is written as

$$
\begin{aligned}
\dot{\mathcal{V}}_4 \leqslant& -c_1 k_1 e_Y^2 - c_2 k_2 e_2^2 - c_3 k_3 e_3^2 + k_1 V_a e_Y \delta_1 + k_2 \frac{g}{V_a} e_2 \delta_2 + \frac{k_2}{\omega_1} e_2 \delta_1 + (\frac{1}{2} - k_\sigma)\sigma_{x1}^2 \\
& + \frac{k_3}{\omega_2} e_3 \delta_2 + [1,1]k_1 \epsilon_1 C_\omega |Q_\omega|^* s_\omega - \frac{\delta_1^2}{\omega_1} + \bar{\delta}_1 \bar{x}_1^d - \frac{\delta_2^2}{\omega_2} + \bar{\delta}_2 \bar{x}_2^d - k_1 V_a e_Y \sigma_{x1} \\
& + s_\omega^{\mathrm{T}} (R_\omega \Gamma_\omega + \Gamma_\omega^{\mathrm{T}} R_\omega + 2\eta_\omega R_\omega R_\omega)s_\omega + \left\||P_\omega|^* B_\omega \bar{\Delta}_\omega\right\|^2 / \eta_\omega \\
\leqslant& \lambda_{\max}(\Xi_C, \Xi_D)\mathcal{V}_4 + \bar{\delta}_1 \bar{x}_1^d + \bar{\delta}_2 \bar{x}_2^d + \left\||P_\omega|^* B_\omega \bar{\Delta}_\omega\right\|^2 / \eta_\omega
\end{aligned}
\tag{53}
$$

By further considering (48), we can scale inequality (53) as

$$
\dot{\mathcal{V}}_4 \leqslant -a\mathcal{V}_4 + b
\tag{54}
$$

where $a = -\lambda_{\max}(\Xi_C, \Xi_D)$ and $b = \bar{\delta}_1 \bar{x}_1^d + \bar{\delta}_2 \bar{x}_2^d + \left\||P_\omega|^* B_\omega \bar{\Delta}_\omega\right\|^2 / \eta_\omega$.

By solving the differential equation, the following inequality is obtained:

$$
\mathcal{V}_4 \leqslant (\mathcal{V}_4(0) - \frac{b}{a})e^{-at} + \frac{b}{a}, t \geqslant 0
\tag{55}
$$

When matrix Ξ_C and Ξ_D are negative, $a = -\lambda_{\max}(\Xi_C, \Xi_D) > 0$, we obtain

$$
\mathcal{V}_4 \leqslant \frac{b}{a}, (t \to \infty)
\tag{56}
$$

According to the definition of $\mathcal{V}_4$ in (51) and inequality (52), we know that by choosing appropriate parameters, the path-following error finally converges to a neighborhood of the origin. This completes the proof.　□

In view of the many design parameters of the above control scheme, the feasibility of the controller is analyzed in combination with the stability condition (48), and the influence of the parameter design on the performance of the closed-loop system is summarized as follows: Considering the unit and order of magnitude, the value of k_1 should be far less than k_2 and k_3. Since the pair (A_ω, C_ω) satisfies the observable condition, there always exists an observer gain matrix L_ω satisfying the stability condition (48) for any given ϵ_1. The controller parameters c_1, c_2, and c_3 are the feedback gains of the controller, which determine the response speed of each loop. From the practical insight of the UAV, the response speed of ϕ is greater than ψ_e, and the response speed of ψ_e is faster than Y_F. Nevertheless, once c_3 is too large, it will increase the burden of the UAV attitude loop. The smaller the filter coefficients ω_1 and ω_2, the smaller the filtering error. However, this will cause the system to overshoot.

Remark 5. *The proposed method using active anti-disturbance technology possesses more anti-disturbance capability compared with the classical robust methods such as those developed in previous studies [20,39,48]. The disturbance estimation would also provide freedom for users to select control gains. Meanwhile, compared with previous trajectory-tracking methods [3,4,28], the proposed path-following method eliminates the speed constraint and provides convenience for the speed control of the fixed-wing UAV.*

4. Simulations

In this section, we provide the simulation results to verify the effectiveness of the path-following strategy based on the DIOB. The prescribed path-generation method is not the focus of this paper (the specific method can be found in [49]), and the UAV parameters used in the simulation were defined according to [1].

In terms of (2), we designed the system matrix A_ω, the input matrix B_ω, and the output matrix C_ω of the exogenous system. Considering the dynamics of the wind disturbance, there were oscillatory and damping modes for each direction of the wind disturbance. Therefore, we used a fourth-order system to simulate the disturbances in two different directions simultaneously, and a second-order system simulated the wind disturbances in each direction. The poles of the system were configured at $[-0.48251, -2.000 \pm 1.414i, -3.517]$. Furthermore, taking into account the coupling effect of the two directions of disturbance, the matrix of the exogenous system was designed as follows:

$$
A_\omega = \begin{bmatrix} 0 & 1 & 0 & 0 \\ -3 & -4 & 1 & 0 \\ 0 & -1 & 0 & 1 \\ 0 & 0 & -3 & -4 \end{bmatrix}, B_\omega = \begin{bmatrix} 0 & 0 \\ 1 & 0 \\ 0 & 0 \\ 0 & 1 \end{bmatrix}, C_\omega = \begin{bmatrix} 1 & 0 & 0 & 0 \\ 0 & 0 & 1 & 0 \end{bmatrix}
$$

According to Section 3.1, the parameters of the DIOB were selected as

$$
L_\omega = \begin{bmatrix} 16.2614 & -0.0949 \\ 34.5782 & 0.4160 \\ -0.0896 & 16.3386 \\ 37.0269 & 34.4678 \end{bmatrix}, P_\omega = \begin{bmatrix} -371.3692 & 18.0876 & -262.8437 & 43.8073 \\ -39.4641 & 16.2636 & 59.7440 & -9.7941 \\ 388.2665 & -23.7900 & 240.7687 & -38.8337 \\ 23.5667 & -9.5612 & -36.6690 & 5.8205 \end{bmatrix}
$$

The control gains in the DIOB-based path-following control law in Section 3.2 were selected as $c_1 = 1$, $c_2 = 5$, $c_3 = 8$. The parameters of filters were selected as $\omega_1 = 1$, $\omega_2 = 1$. The parameters of the auxiliary system were selected as $k_\sigma = 0.5$, $\mu = 0.1$. The purpose of this scenario was to drive the UAV to follow an irregular path. The speed of the UAV was kept at a constant 30 m/s. The UAV was started from location $(0, 0)$. In this section, three different types of disturbances are analyzed for simulation verification.
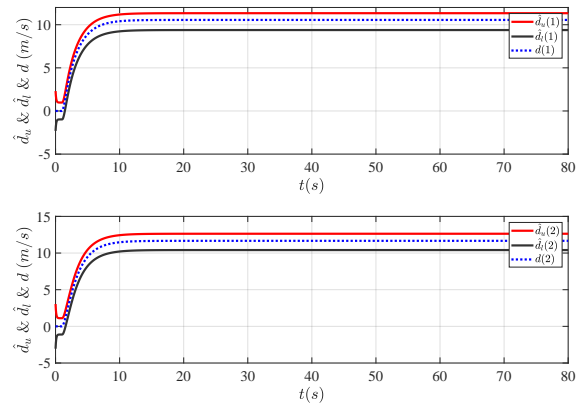
Case 1 (Step Wind Disturbances): The inputs of the exogenous system (2) are step signals, which are used to simulate the continuous constant wind disturbance of UAV. The path-following performance is shown in Figure 4a. It shows that the controller can stably follow the prescribed path. To clearly show the difference, we show the path-following error in the $\mathcal{F}$ frame in Figure 4b. The UAV with the DIOB-based path-following controller can follow the prescribed path faster and more stably. Moreover, the steady-state path-following error is smaller than the UAV without the DIOB controller. Figure 5a shows the heading angle and the roll angle of the UAV. The estimation errors of DIOB are shown in Figure 5b. Figure 6 shows the state of the auxiliary system, the virtual control law x_1^d, and so on. We see that command x_1^d is saturated before 9 s, which changes the state σ_{x1} of the auxiliary system.
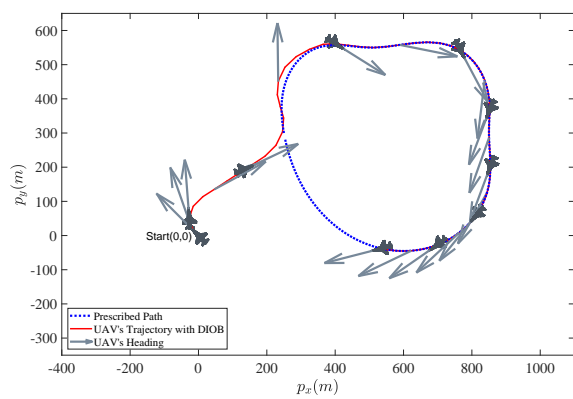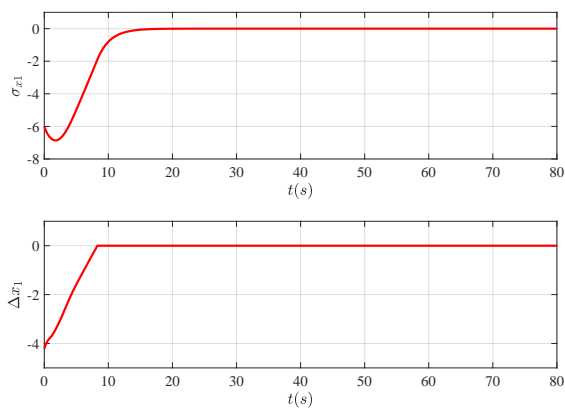
(a) Prescribed path and UAV trajectory
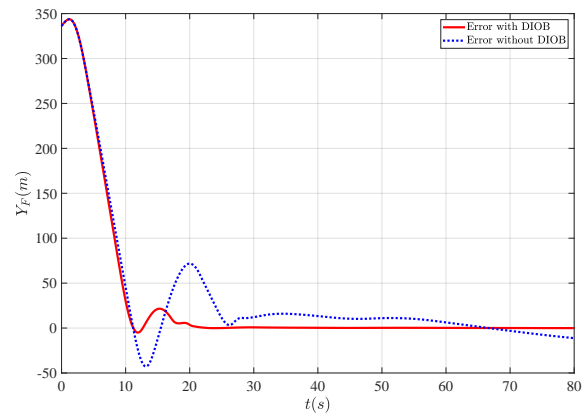
(b) Path-following error in $\mathcal{F}$

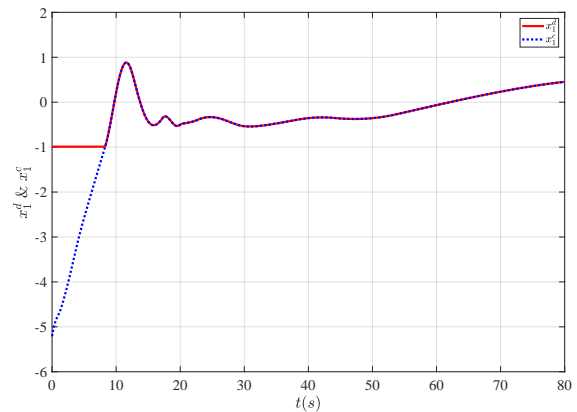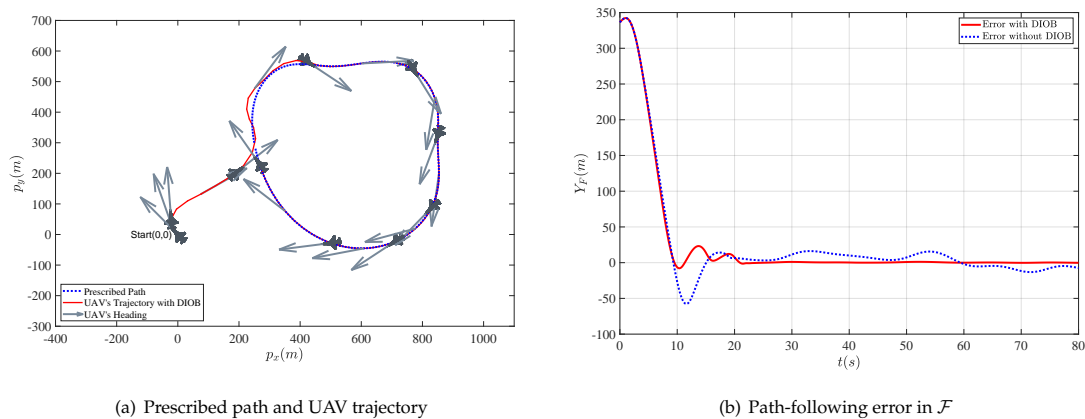**Figure 4.** Case 1: UAV trajectory and path-following error.
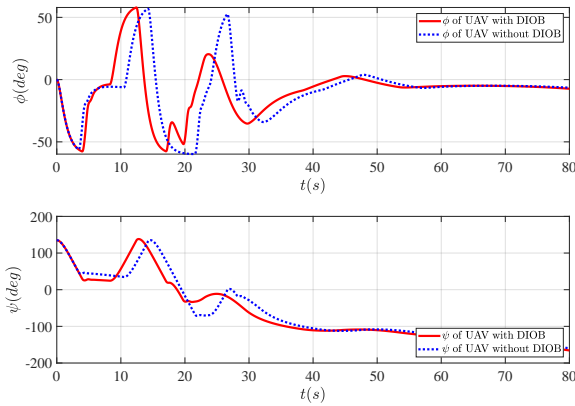
(a) Closed-loop Signals of UAV

(b) Interval Estimation of DIOB

Figure 5. Case 1: Closed-loop signals of UAV and interval estimation of DIOB.

(a) Responses of auxiliary system

(b) Command limitation on heading angle

Figure 6. Case 1: Responses of auxiliary system and command limitation on heading angle.

Case 2 (Sinusoidal Wind Disturbances): The inputs of the exogenous system (2) are sinusoidal signals. Compared with case 1, the disturbance signals are multi-frequency sinusoidal signal combinations. This case simulates the dynamic disturbance of UAV

during flight. The path-following performance and path-following error in $\mathcal{F}$ are shown in Figure 7a,b, respectively. The path-following performance of the UAV did not change significantly. The UAV could still follow the prescribed path stably, quickly, and accurately. Figure 8a,b show the heading angle and the roll angle of the UAV and the outputs of the DIOB. The state of auxiliary and the virtual control law x_1^d and x_1^c are shown in Figure 9. Two times of saturation occurred in 0–5 s and about 10 seconds, respectively. The auxiliary system effectively enhanced the stability of the closed-loop system under the command limitation.

(a) Prescribed path and UAV trajectory

(b) Path-following error in $\mathcal{F}$

Figure 7. Case 2: UAV trajectory and path-following error.
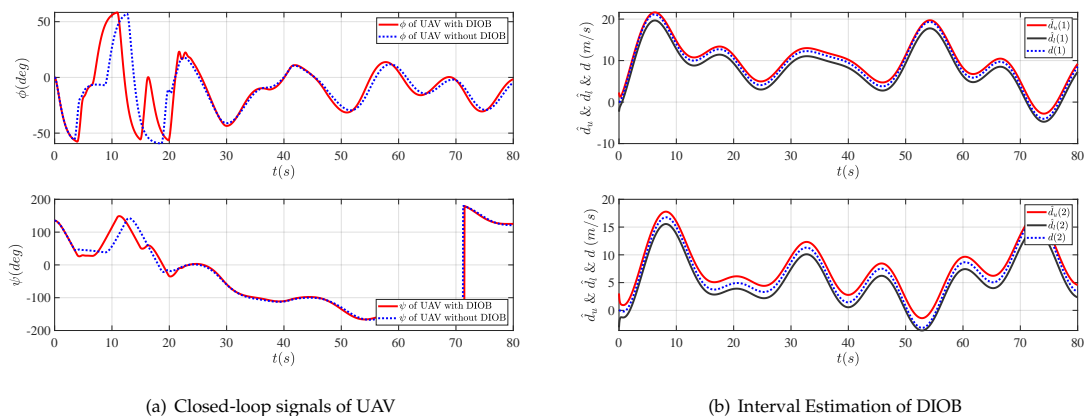

(a) Closed-loop signals of UAV

(b) Interval Estimation of DIOB

Figure 8. Case 2: Closed-loop signals of UAV and the interval estimation of DIOB.

(a) Responses of auxiliary system

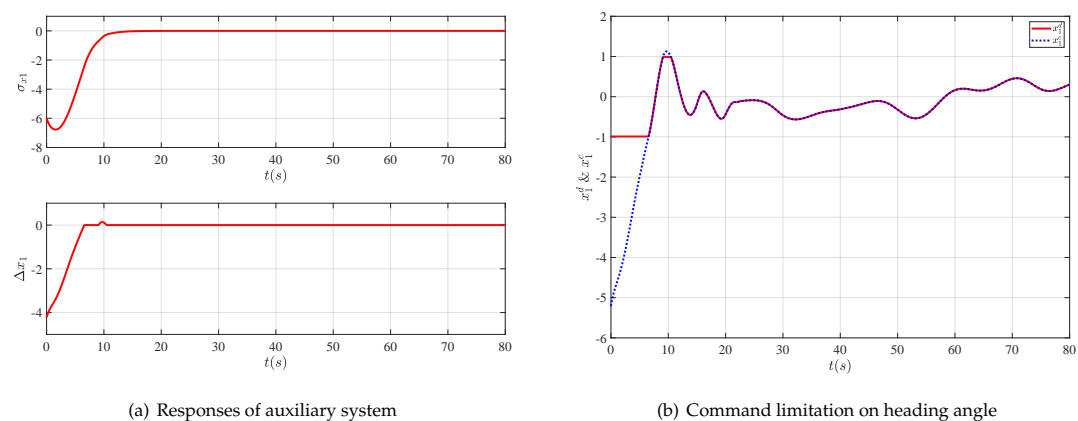(b) Command limitation on heading angle

Figure 9. Case 2: Responses of the auxiliary system and command limitation on the heading angle.

Case 3 (Comparison Study): To show the proposed method's characteristics more intuitively, we selected a more complicated path for simulation research. In addition, for this case, we selected some common path-following methods for comparative study, including the VTP based on the geometric method, the LQI, and the classical disturbance observer-based control (DOBC). In the simulation, we used the motion model proposed in (1) uniformly. The wind disturbance, in this case, was the same as that in case 2. Figure 10 shows the tracking and following error comparison of the different methods. It can be seen from Figure 10a that the four methods used could stably follow the reference path. Figure 10b shows a clear comparison of the path-following error of the various methods. In the wind disturbance environment, the effect of the VTP method was the worst, closely followed by the LQI. Obviously, in this scenario, the DOBC method and DIOB method were better than the former two methods. Since both the DIOB and DOBC use the estimated disturbance information as feedforward control, their performance was very close. However, we can see that the anti-disturbance ability of the DIOB method was slightly better than that of the DOBC, as shown in Figure 10b.
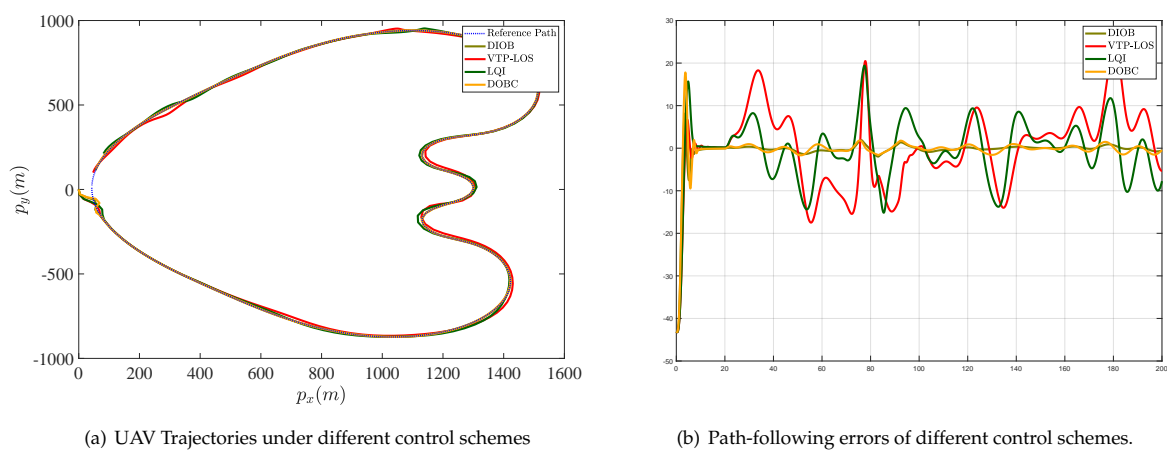

(a) UAV Trajectories under different control schemes

(b) Path-following errors of different control schemes.

Figure 10. Case 3: UAV Trajectories and path-following errors of different control schemes.

In order to show the performance of various methods more intuitively, we selected two performance indexes for comparison. One is the integration of the absolute value of the error $\Delta_{error} = \int_0^{t_{end}} |Y_F| \, dt$, and the other is the integration of the absolute value of the system input $\Delta_u = \int_0^{t_{end}} |u| \, dt$, where t_{end} is the end time of the simulation. Δ_{error} measures the path-following error, and Δ_u measures the energy consumption of the system. The performance indexes of case 3 are shown in Table 1. It can be seen that, in this case, the error indexes of the DIOB method and the DOBC method schemes were far less than the other two, and the energy consumption of the DIOB method was slightly less than that of the DOBC method.

Table 1. Performance indices of case 3.

Names of Methods	Δ_{error}	Δ_u
DIOB	176.0	65.1
VTP	1448.6	62.6
LQI	1044.2	65.8
DOBC	230.6	67.6

Overall, the path-following control method of UAVs based on the DIOB can address various forms of external disturbances and different forms of reference paths. Compared with the general path-following control strategy, it shows better path-following performance in the specific situation.

5. Summary

In this work, we presented the robust constrained path-following control scheme for UAVs under wind disturbances. By appointing the projection from the UAV to the path, the Serret–Frenet frame was introduced, and the complexity of the path-following problem was reduced. Specifically, the DIOB was employed, and it proved capable of generating the upper and lower boundaries of the wind disturbances. The path-following control design was presented based on the dynamic surface control technique, and the auxiliary system was adopted to address the command limitation. Theoretical analysis revealed the design conditions and feasibility endurance. The effectiveness of the developed control scheme was demonstrated with numerical simulations. It is worth highlighting that there are still many unexplored research avenues for the path-following problem in UAVs. For example, the 3 or 4 dimensional path-following control methods of UAVs should be taken into consideration in the future. The modeling for wind disturbance in this paper is relatively simple. In addition, the UAV path-following control under random wind disturbance is still a challenge.

Data Availability Statement: Not applicable.

Conflicts of Interest: The authors declare no conflict of interest.

References

1. Beard, R.W.; McLain, T.W. *Small Unmanned Aircraft: Theory and Practice*; Princeton University Press: Princeton, NJ, USA, 2012.
2. Yong, K. Disturbance interval observer-based carrier landing control of unmanned aerial vehicles using prescribed performance. *Sci. Sin. Informationis* **2022**, *52*, 1711. [CrossRef]
3. Chen, M.; Xiong, S.; Wu, Q. Tracking flight control of quadrotor based on disturbance observer. *IEEE Trans. Syst. Man Cybern. Syst.* **2019**, *51*, 1414–1423. [CrossRef]
4. Ye, H.; Chen, M.; Zeng, Q. Horizontal motion tracking control for an underwater vehicle with environmental disturbances. In Proceedings of the 2017 36th Chinese Control Conference (CCC), Dalian, China, 26–28 July 2017; pp. 4952–4957. [CrossRef]
5. Yong, K.; Chen, M.; Wu, Q. Immersion and invariance-based integrated guidance and control for unmanned aerial vehicle path following. *Int. J. Syst. Sci.* **2019**, *50*, 1052–1068. [CrossRef]
6. Beard, R.W.; Ferrin, J.; Humpherys, J. Fixed wing UAV path following in wind with input constraints. *IEEE Trans. Control. Syst. Technol.* **2014**, *22*, 2103–2117. [CrossRef]
7. Aguiar, A.P.; Hespanha, J.P.; Kokotovic, P.V. Path-following for nonminimum phase systems removes performance limitations. *IEEE Trans. Autom. Control* **2005**, *50*, 234–239. [CrossRef]
8. Aguiar, A.P.; Hespanha, J.P. Trajectory-tracking and path-following of underactuated autonomous vehicles with parametric modeling uncertainty. *IEEE Trans. Autom. Control* **2007**, *52*, 1362–1379. [CrossRef]
9. Park, S.; Deyst, J.; How, J.P. Performance and lyapunov stability of a nonlinear path following guidance method. *J. Guid. Control Dyn.* **2007**, *30*, 1718–1728. [CrossRef]
10. Kaminer, I.; Pascoal, A.; Xargay, E.; Hovakimyan, N.; Cao, C.; Dobrokhodov, V. Path following for small unmanned aerial vehicles using L1 adaptive augmentation of commercial autopilots. *J. Guid. Control Dyn.* **2010**, *33*, 550–564. [CrossRef]
11. Nelson, D.R.; Barber, D.B.; McLain, T.W.; Beard, R.W. Vector field path following for miniature air vehicles. *IEEE Trans. Robot.* **2007**, *23*, 519–529. [CrossRef]
12. Chen, H.; Chang, K.; Agate, C.S. UAV path planning with tangent-plus-Lyapunov vector field guidance and obstacle avoidance. *IEEE Trans. Aerosp. Electron. Syst.* **2013**, *49*, 840–856. [CrossRef]
13. Frew, E.W.; Lawrence, D. Tracking dynamic star curves using guidance vector fields. *J. Guid. Control Dyn.* **2017**, *40*, 1488–1495. [CrossRef]
14. Xargay, E.; Kaminer, I.; Pascoal, A.; Hovakimyan, N.; Dobrokhodov, V.; Cichella, V.; Aguiar, A.P.; Ghabcheloo, R. Time-critical cooperative path following of multiple unmanned aerial vehicles over time-varying networks. *J. Guid. Control Dyn.* **2013**, *36*, 499–516. [CrossRef]

15. Furieri, L.; Stastny, T.; Marconi, L.; Siegwart, R.; Gilitschenski, I. Gone with the wind: Nonlinear guidance for small fixed-wing aircraft in arbitrarily strong windfields. In Proceedings of the 2017 American Control Conference (ACC), Seattle, WA, USA, 24–26 May 2017; pp. 4254–4261. [CrossRef]

16. Gavilan, F.; Vazquez, R.; Camacho, E.F. An iterative model predictive control algorithm for UAV guidance. *IEEE Trans. Aerosp. Electron. Syst.* **2015**, *51*, 2406–2419. [CrossRef]

17. Fan, Y.; Zou, X.; Wang, G.; Mu, D. Robust Adaptive Path Following Control Strategy for Underactuated Unmanned Surface Vehicles with Model Deviation and Actuator Saturation. *Appl. Sci.* **2022**, *12*, 2696. [CrossRef]

18. Huang, Y.; Shi, X.; Huang, W.; Chen, S. Internal Model Control-Based Observer for the Sideslip Angle of an Unmanned Surface Vehicle. *J. Mar. Sci. Eng.* **2022**, *10*, 470. [CrossRef]

19. Yong, K.; Chen, M.; Wu, Q. Noncertainty-equivalent observer-based noncooperative target tracking control for unmanned aerial vehicles. *Sci. China Inf. Sci.* **2022**, *65*, 152202. [CrossRef]

20. Manchester, I.R.; Savkin, A.V. Circular navigation missile guidance with incomplete information and uncertain autopilot model. *J. Guid. Control Dyn.* **2004**, *27*, 1078–1083. [CrossRef]

21. Feng, Z.; Pan, Z.; Chen, W.; Liu, Y.; Leng, J. USV Application Scenario Expansion Based on Motion Control, Path Following and Velocity Planning. *Machines* **2022**, *10*, 310. [CrossRef]

22. Patrikar, J.; Makkapati, V.R.; Pattanaik, A.; Parwana, H.; Kothari, M. Nested saturation based guidance law for unmanned aerial vehicles. *J. Dyn. Syst. Meas. Control* **2019**, *141*, 071008. [CrossRef]

23. Kukreti, S.; Kumar, M.; Cohen, K. Genetically tuned LQR based path following for UAVs under wind disturbance. In Proceedings of the 2016 International Conference on Unmanned Aircraft Systems (ICUAS), Arlington, VA, USA, 7–10 June 2016; pp. 267–274. [CrossRef]

24. Liang, Y.; Jia, Y.; Wang, Z.; Matsuno, F. Combined vector field approach for planar curved path following with fixed-wing UAVs. In Proceedings of the 2015 American Control Conference (ACC), Chicago, IL, USA, 1–3 July 2015; pp. 5980–5985. [CrossRef]

25. Rucco, A.; Aguiar, A.P.; Pereira, F.L.; de Sousa, J.B. A predictive path-following approach for fixed-wing unmanned aerial vehicles in presence of wind disturbances. In Proceedings of the Robot 2015: Second Iberian Robotics Conference, Lisbon, Portugal, 19–21 November 2015; Springer: Cham, Switzerland, 2016; pp. 623–634. [CrossRef]

26. Gao, J.; Wang, P.; Tang, Z. An Accurate Path Following Algorithm of UAVs Under Crosswind Disturbance. *Int. Conf. Auton. Unmanned Syst.* **2021**, 1717–1727. [CrossRef]

27. Tanaka, K.; Tanaka, M.; Takahashi, Y.; Iwase, A.; Wang, H.O. 3-D flight path tracking control for unmanned aerial vehicles under wind environments. *IEEE Trans. Veh. Technol.* **2019**, *68*, 11621–11634. [CrossRef]

28. Zhang, Y.; Chen, Z.; Sun, M.; Zhang, X. Trajectory tracking control of a quadrotor UAV based on sliding mode active disturbance rejection control. *Nonlinear Anal. Model. Control* **2019**, *24*, 545–560. [CrossRef]

29. Cabecinhas, D.; Cunha, R.; Silvestre, C. A globally stabilizing path following controller for rotorcraft with wind disturbance rejection. *IEEE Trans. Control Syst. Technol.* **2014**, *23*, 708–714. [CrossRef]

30. Brezoescu, A.; Espinoza, T.; Castillo, P.; Lozano, R. Adaptive trajectory following for a fixed-wing UAV in presence of crosswind. *J. Intell. Robot. Syst.* **2013**, *69*, 257–271. [CrossRef]

31. Chen, M.; Chen, W.H. Sliding mode control for a class of uncertain nonlinear system based on disturbance observer. *Int. J. Adapt. Control Signal Process.* **2010**, *24*, 51–64. [CrossRef]

32. Li, R.; Chen, M.; Wu, Q. Adaptive neural tracking control for uncertain nonlinear systems with input and output constraints using disturbance observer. *Neurocomputing* **2017**, *235*, 27–37. [CrossRef]

33. Yang, G.; Yao, J.; Dong, Z. Neuroadaptive learning algorithm for constrained nonlinear systems with disturbance rejection. *Int. J. Robust Nonlinear Control* **2022**. [CrossRef]

34. Liu, C.; McAree, O.; Chen, W.H. Path-following control for small fixed-wing unmanned aerial vehicles under wind disturbances. *Int. J. Robust Nonlinear Control* **2013**, *23*, 1682–1698. [CrossRef]

35. Shao, S.; Chen, M. Robust discrete-time fractional-order control for an unmanned aerial vehicle based on disturbance observer. *Int. J. Robust Nonlinear Control* **2022**, *32*, 4665–4682. [CrossRef]

36. Yang, G. Asymptotic tracking with novel integral robust schemes for mismatched uncertain nonlinear systems. *Int. J. Robust Nonlinear Control* **2022**, *33*, 1988–2002. [CrossRef]

37. Yong, K.; Chen, M.; Shi, Y.; Wu, Q. Hybrid estimation strategy-based anti-disturbance control for nonlinear systems. *IEEE Trans. Autom. Control* **2020**, *66*, 4910–4917. [CrossRef]

38. Yong, K.; Chen, M.; Wu, Q. Anti-disturbance control for nonlinear systems based on interval observer. *IEEE Trans. Ind. Electron.* **2019**, *67*, 1261–1269. [CrossRef]

39. Zhao, Y.; Dong, L. Robust path-following control of a container ship based on Serret–Frenet frame transformation. *J. Mar. Sci. Technol.* **2020**, *25*, 69–80. [CrossRef]

40. Liu, C.; McAree, O.; Chen, W.H. Path following for small UAVs in the presence of wind disturbance. In Proceedings of 2012 UKACC International Conference on Control, Cardiff, UK, 3–5 September 2012; pp. 613–618. [CrossRef]

41. Murray, R.M.; Li, Z.; Sastry, S.S. *A Mathematical Introduction to Robotic Manipulation*; CRC Press: Boca Raton, FL, USA, 2017.

42. Zhao, S.; Wang, X.; Zhang, D.; Shen, L. Curved path following control for fixed-wing unmanned aerial vehicles with control constraint. *J. Intell. Robot. Syst.* **2018**, *89*, 107–119. [CrossRef]

43. Poksawat, P.; Wang, L.; Mohamed, A. Gain scheduled attitude control of fixed-wing UAV with automatic controller tuning. *IEEE Trans. Control. Syst. Technol.* **2017**, *26*, 1192–1203. [CrossRef]
44. Polycarpou, M.M.; Ioannou, P.A. A robust adaptive nonlinear control design. In Proceedings of the 1993 American Control Conference, San Francisco, CA, USA, 2–4 June 1993; pp. 1365–1369. [CrossRef]
45. Gouzé, J.L.; Rapaport, A.; Hadj-Sadok, M.Z. Interval observers for uncertain biological systems. *Ecol. Model.* **2000**, *133*, 45–56. [CrossRef]
46. Chen, M.; Ge, S.S.; Ren, B. Adaptive tracking control of uncertain MIMO nonlinear systems with input constraints. *Automatica* **2011**, *47*, 452–465. [CrossRef]
47. Zheng, X.; Yang, X. Command filter and universal approximator based backstepping control design for strict-feedback nonlinear systems with uncertainty. *IEEE Trans. Autom. Control* **2019**, *65*, 1310–1317. [CrossRef]
48. Wang, R.; Jing, H.; Hu, C.; Yan, F.; Chen, N. Robust H_∞ Path Following Control for Autonomous Ground Vehicles With Delay and Data Dropout. *IEEE Trans. Intell. Transp. Syst.* **2016**, *17*, 2042–2050. [CrossRef]
49. Valavanis, K.P.; Vachtsevanos, G.J. *Handbook of Unmanned Aerial Vehicles*; Springer: Berlin/Heidelberg, Germany, 2015; Volume 1.